Title

Probing the effect of atomic and morphological arrangements in the pseudocapacitive properties of TT-Nb2O5 nanostructures

Journal

Solid State Ionics, 429

ISSN

0167-2738

Authors

Zambotti, Andrea
Nkala, Gugulethu Charmaine
Dutta, Supriti
et al.

Publication Date

2025-10-01

DOI

10.1016/j.ssi.2025.116990

Probing the effect of atomic and morphological arrangements in the pseudocapacitive properties of *TT*-Nb_2O_5 nanostructures

Andrea Zambotti[1], Gugulethu Charmaine Nkala[2], Supriti Dutta[3], Sree Harsha Bhimineni[3], Nicolas Leport[4], Aimeric Laperruque[4], Johanna Nelson Weker[2], Philippe Sautet[3], Laurent Pilon[4], Bruce Dunn[1]

[1]Department of Materials Science and Engineering, University of California, Los Angeles 90095 California, United States

[2]Stanford Synchrotron Radiation Lightsource, SLAC National Accelerator Laboratory, Menlo Park, California 94025, United States

[3]Department of Chemical and Biomolecular Engineering, University of California, Los Angeles 90095 California, United States

[4]Mechanical and Aerospace Engineering Department, Henry Samueli School of Engineering and Applied Science, University of California, Los Angeles, CA 90095, USA

Abstract

In this study, we determine the role of oxygen vacancies and preferred surface orientation on the charge storage properties of the lithium intercalation host, pseudohexagonal *TT*-Nb_2O_5. Two different morphologies were synthesized, namely nanosheets and nanowires. We employed a set of advanced characterization techniques including entropic potential measurements, high-resolution synchrotron X-ray diffraction and synchrotron X-ray absorption spectroscopy together with electrochemical measurements and density functional theory calculations. Our results indicate that the two morphologies exhibit different oxygen vacancy characteristics as nanosheets have oxygen vacancies limited to the surface while nanowires possess vacancies which tend to be located in the bulk solid. Oxygen vacancies in the bulk of *TT*-Nb_2O_5 lead to an appreciable increase in specific capacity compared to nanosheets where oxygen vacancies confined to specific crystallographic surfaces do not make a significant contribution to the electrochemical response of the *TT*-Nb_2O_5 anodes. These results show how the distribution and concentration of oxygen vacancies play a major role in the lithiation mechanisms of *TT*-Nb_2O_5.

Keywords: *TT-Nb_2O_5, Lithium ion batteries, lithium insertion, Entropic potential, Synchrotron XRD, XAS, Density Functional Theory*

1. Introduction

Research on materials for electrochemical energy storage has received enormous interest over the past decade in response to significant growth in the demand for consumer electronics, grid energy storage and electrified transportation. The development of engineered electrodes which are able to deliver high energy density at high power densities is a particularly important challenge for the transportation sector, which alone accounts for 28% of US greenhouse gas emissions.[1,2] To achieve this combination of high energy and power densities, materials featuring intercalation pseudocapacitance have attracted considerable attention as their kinetic responses are comparable to those of electric double layer capacitors while their energy storage properties arise from intercalation processes and the accompanying redox reactions.[3–5] Fast cation insertion is enabled by storing ions in interstitial sites of the crystalline network without undergoing first order phase transitions (i.e., forming solid solutions). Accordingly, these materials are generally not kinetically limited by semi-infinite diffusion of lithium, and most importantly, their cyclability is greatly improved by the limited volumetric variations that are typical of solid solution regimes upon charge and discharge cycles. In recent years, a number of crystalline compounds have been reported to display Li^+ intercalation that can be associated with a pseudocapacitive response, such as *T*-Nb_2O_5 and some of its polymorphs, as well as various Wadsley-Roth shear phases like $V_7Nb_6O_{29}$, $Nb_{18}W_8O_{69}$ or $Mo_3Nb_2O_{14}$.[6–9] A common feature of these compounds is their promise as high potential anodes that intercalate lithium at a voltage lower than the LUMO of the electrolyte, thus avoiding the formation of the solid electrolyte interface. In turn, this characteristic affects the overall energy density by constricting the working potential window, so that great efforts have been made to decrease the lithium insertion potential of these anode materials via chemical and/or structural modifications while preserving their advantageous kinetics.[10]

In contrast to conventional layered compounds that intercalate lithium, *T*-Nb_2O_5 possesses a pillared structure due to the presence of oxygen bridges along the *c*-direction of the unit cell that prevent the formation of Li^+ slabs upon intercalation.[11] This rigid framework leads to a crystal structure that can host Li^+ without undergoing any first order phase transition in the $0<x<0.8$ $Li_xNb_2O_5$ range, while also undergoing an insulator to metallic conductor transition upon filling of the Nb 4*d* orbitals.[12] Moreover, the degree of crystallinity has proven to be equally important for its stability and performance. As Nb_2O_5 transitions from amorphous to *TT*-Nb_2O_5 to *T*-Nb_2O_5 upon raising the synthesis temperature, the overall lithium uptake and its cyclability increase.[13] Recently, research groups demonstrated that oxygen vacancies can be selectively introduced in T-Nb_2O_5 to enhance its electrochemical performances by mitigating Jahn-Teller distortions while improving the electronic conductivity of the crystalline structure.[14,15] This kind of chemical modification has been shown to give rise to extrinsic pseudocapacitive properties, as demonstrated in layered MoO_{3-x}.[16] On the other hand, there is evidence of detrimental effects as oxygen-deficient structures have been shown to undergo irreversible redox reactions and structural transformations due to the high affinity of Li^+ to vacancy sites.[17] These examples give an overview of the fundamental questions regarding the complicated interplay of structural, morphological and chemical features that allows nearly theoretical amounts of lithium to be reversibly (de)inserted in a solid-solution regime.

In the study reported here, our overarching objective is to establish the role of oxygen vacancies in the charge storage properties of *TT*-Nb_2O_5. We found *TT*-Nb_2O_5 to be an excellent candidate for this study as it enables us to synthesize highly anisotropic nanostructures without undergoing sintering. Moreover, we have the ability to tune the distribution of oxygen vacancies by using capping agents to target unconventional and defective crystal growth. It is important to note that the *TT*-Nb_2O_5 pseudohexagonal phase is inherently oxygen-defective as compared to its orthorhombic polymorph, *T*-Nb_2O_5, making it a suitable candidate for this study. The combination of synchrotron techniques such as high-resolution X-ray diffraction (XRD) and X-ray absorption spectroscopy (XAS) together with electrochemical measurements and theoretical calculations show the influence of morphology and defect chemistry on the electrochemical properties of *TT*-Nb_2O_5.

Materials and methods

Synthesis of TT-Nb_2O_5 nanostructures

Nanosheets were synthesized by modifying a published procedure.[18] Briefly, 23.3 ml of ethylenediamine (Sigma-Aldrich) was mixed with 11.7 ml of deionized water, then 210 mg of $NbCl_5$ (Alfa Aesar) was slowly added to the solution and stirred for 30 minutes. The mixture was then transferred to a 45 ml PTFE lined hydrothermal reactor (Model 4744, Parr Inst. Co) and heated to and held at 190°C for 24 h. The resulting precipitate was thoroughly washed with ethanol, centrifuged and air dried prior to heat treating it at 500°C in air (5°C·min^{-1} for 3 h, air cooled at ~20°C·min^{-1}).

Nanowires were also synthesized by hydrothermal reactions as we modified another published procedure.[19]. In this case, 218 mg of $NbCl_5$ was first mixed with 20 ml of deionized water under vigorous stirring. Then, 500 mg of oxalic acid dihydrate (Sigma-Aldrich) was added and the solution was mixed until it turned transparent, at which point 280 mg of hexamethylenetetramine (ThermoFisher Scientific) were added. The mixture was sealed in a 45 ml hydrothermal reactor and heat treated at 180°C for 14 h. The resulting precipitate was then subjected to the same washing, drying and annealing procedure adopted during the nanosheets synthesis.

Characterization techniques

Scanning (SEM) and Transmission Electron Microscopy (TEM) were used to probe the morphological and crystallographic orientations of the synthesized nanostructures, using a NovaTM 230 Nano SEM and an FEI Titan 80-300 scanning transmission electron microscope, respectively. SEM acquisitions were performed with a magnification of 100k, working distance of 5.3 mm, spot size of 3.5 and 15 kV accelerating voltage. TEM micrographs were obtained at a magnification of 300k with an accelerating voltage of 300 kV. Raman spectra of the pristine *TT*-Nb_2O_5 nanostructures were acquired with an inVia™ Renishaw confocal Raman microscope equipped with a 514 nm green laser in the 0-1200 cm^{-1} range.

High-resolution XRD was used to determine the average structure of *TT*-Nb_2O_5 nanoarchitectures and establish their preferred growth directions. The data presented in this work were obtained through the mail-in robotic XRD program at BL 2-1 at Stanford Synchrotron Radiation Lightsource (SSRL) with an incident X-ray energy of 16.99 keV (λ = 0.7295 Å).[20] Detailed information on the measurement setup and the Rietveld refinement results can be found in the *Supplemental Information*. The resulting crystal structures were visualized in the VESTA software.[21]

XAS provided insights into the oxidation state, coordination geometry and the effect of nanoarchitecture on the oxygen vacancies that govern the pseudocapacitive properties of TT-Nb_2O_5. Nb K-edge spectra were measured across the edge (18 986 eV) and collected at BL 4-1 at SSRL at ambient conditions. For qualitative extended X-ray absorption fine structure (EXAFS) analysis, phase uncorrected K-edge spectra were converted to χ (k) and subsequently Fourier transformed (FT) to χ (R) to yield the radial distribution function. The k-range for FT was 3.0 to 12.0 $Å^{-1}$, with dk of 1 using a Hanning window and an arbitrary k-weight of 0.5. A *T*-Nb_2O_5 reference oxide standard was used. More information on the XAS measurements setup, reference oxide and sample preparation is presented in the *Supplemental Information*.

Periodic Density Functional Theory (DFT) computations were performed on crystal structures experimentally determined by Rietveld refinement using the Vienna Ab initio Simulation Package (VASP).[22] To account for van der Waals interactions, the exchange-correlation was calculated using the Perdew–Burke–Ernzerhof (PBE) functional in the generalized gradient approximation (GGA) in conjunction with the DFT-D3 correction.[23,24] The energy cutoff was set to 400 eV. The projector augmented wave (PAW) approach was used to model interactions between electrons and atomic cores.[25] Initial geometric optimizations were carried out in vacuum until the total energy converged to less than 10–6 eV and the forces acting on each atom were less than 0.01 eV $Å^{-1}$. Then, geometry optimizations were carried out with implicit solvation through VASPsol with convergence requirements of 10-6 eV for energy and 0.02 eV $Å^{-1}$ for forces.[26] The details of theoretical background utilized in performing DFT analyses are provided in a dedicated section of the *Supplemental Information*, together with the methodology adopted to model the *TT*-Nb_2O_5 defective surfaces.

Electrode fabrication and testing

All electrochemical tests were performed in a 2-electrode configuration using 304 Stainless Steel-CR2032 coin cells, metallic lithium counter electrodes, glass fiber separators and 1M $LiClO_4$ in propylene carbonate (Sigma-Aldrich) electrolyte. Working electrodes were fabricated by mixing mass fractions of 80% active material, 5% C65 carbon (MTI Corp.), 5% multi-walled carbon nanotubes (MSE Supplies LLC), 5% carboxymethyl cellulose (MSE supplies LLC) and 5% styrene-butadiene rubber (MTI Corp.) into water-based slurries. Every slurry was cast onto carbon-coated aluminum foil via doctor-blading and dried at 80°C in vacuum overnight, resulting in active material mass loadings of ~1 $mg\cdot cm^{-2}$ and electrode thicknesses of ~10-15 μm.

A BioLogic VMP-300 potentiostat was utilized for cyclic voltammetry (CV) and galvanostatic cycling with potential limitation (GCPL) measurements. CV tests were performed with sweep rates between 0.2 $mV\cdot s^{-1}$ and 1.0 $mV\cdot s^{-1}$. GCPL measurements were carried out over the 1.2-3 V vs Li^+/Li voltage range. The C-rates were based on the theoretical capacity of *TT*-Nb_2O_5 (202 $mAh\cdot g^{-1}$ for 1 electron redox).

The open circuit voltage $U_{OCV}(x,T)$ and entropic potential $\partial U_{OCV}(x,T)/\partial T$ of half coin cells made with *TT*-Nb_2O_5 nanosheet or nanowire electrodes were measured as functions of lithium composition at 20 °C using the procedure and arrangement described elsewhere, and based on Galvanostatic Intermittent Titration Technique (GITT).[27] A series of current pulses were imposed at C/10 for 30 minutes, followed by a relaxation period of 270 minutes. At the end of each relaxation, the temperature was changed between 15 °C and 25 °C, with 5 °C steps using a thermoelectric cold plate (TE technology, CP-121). The potential of the cell was recorded using a potentiostat (Biologic, VSP-300). To confirm the cell was in thermodynamic equilibrium, the following two conditions needed to be satisfied: (i) the temperature difference between the cold plate and the top of the cell was less than 0.1 °C and (ii) the time rate of change of the open circuit voltage $\partial U_{OCV}/\partial t$ was less than 1 $mV\cdot h^{-1}$.

Electrochemical impedance spectroscopy (EIS) was performed using a Biologic potentiostat over a frequency range of 100 kHz to 10 mHz with an AC amplitude of 10 mV. Measurements were made at open circuit potential after stabilization. Both *TT*-Nb_2O_5 nanosheet and nanowire electrodes were tested in coin cells with lithium metal as the counter/reference electrode and 1 M $LiClO_4$ in PC as the electrolyte. All experiments were carried out at room temperature after 2 cycles at C/10.

2. Results and discussion

The experimental results focused on determining how preferential crystallographic orientations and the presence of oxygen vacancies contributed to the lithiation of highly anisotropic nanostructures (i.e., nanosheets and nanowires). The cyclic voltammograms in **Figures 1a and 1b** display the typical current-voltage response of pseudocapacitive *TT*-Nb_2O_5 to (de)lithiation, and are characterized by similar Li^+ insertion potentials below 2.0 V.[13,28] By contrast, nanowires respond to lithium intercalation with broad peaks at 1.6-1.7 V in the cathodic and anodic sweeps, respectively. The absence of broad peaks in nanosheets suggests that there is no preferential insertion of Li^+ at that potential. Moreover, *b*-value analysis (**Figure 1c**) reveals clear differences in the kinetics of the two nanostructures. In this analysis, the relation between current and sweep rate (i-v) is given as $i=av^b$, where a and b are a generalized coefficient and exponent, respectively. The *b*-value provides insight regarding the kinetics occurring in the redox process. If the *b*-value falls near 0.5, slow diffusion in a semi-infinite medium is considered to be the controlling factor for the electrochemical process, as generally occurs for battery electrode materials undergoing a phase transition. For $b \to 1$, the kinetics resemble an ideal capacitor (or a pseudocapacitive material in the present case) and are considered to be surface controlled or fast intercalation. Values between 0.5 and 1.0 are described by finite diffusion processes. [29] **Figure 1c** shows that nanowires respond at a faster rate than nanosheets, as the average *b*-values of the two different samples are 0.94 and 0.8, respectively. Moreover, nanosheets result in a markedly slower response upon delithiation (charge) as compared with nanowires. The linear voltage profile of the galvanostatic cycling curves given in **Figure 1d,e** provide additional support of intercalation in a solid-solution as the charge storage mechanism for both morphologies, as similarly observed in other published works.[11,30–33] Interestingly, the nanowires are able to insert nearly 0.8 Li^+ per transition metal center (~160 $mAh \cdot g^{-1}$) at a rate of 0.1C, while nanosheets can only store 0.55 Li^+/Nb (~110 $mAh \cdot g^{-1}$). Additionally, when imposing faster charge/discharge rates, the capacity decrease for nanosheets is more pronounced (**Figure 1f)**. The capacity retention between 0.1C and 10C for nanowires and nanosheets is 62.5% and 36.4%, respectively. Additional results can be derived from long cycling tests at 1C (**Figure S1a**), where nanowires retain 120 $mAh \cdot g^{-1}$ and nanosheets just 72 $mAh \cdot g^{-1}$ after

100 cycles, and from impedance spectroscopy (**Figure S1b**) displaying lower electrode resistance in the case of nanowires.

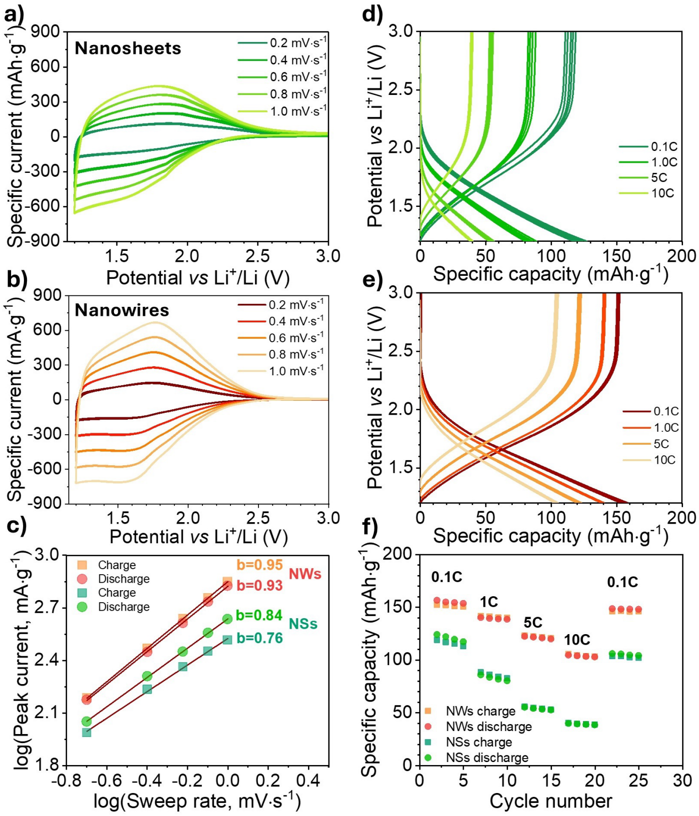

Figure 1: Electrochemical performance of TT-Nb_2O_5 electrodes. a), b): cyclic voltammograms between 0.2 and 1.0 mV·s^{-1}; c) the b-value analysis retrieved from CVs; d), e) galvanostatic cycling between 0.1C and 10C (with respect to the theoretical capacity of 202 mAh·g^{-1} for 1 e^{-} redox); f) rate capability plot in the 0.1-10C range.

We carried out entropic potential measurements on both of the nanostructured *TT*-Nb_2O_5 materials to confirm intercalation in solid-solution as the charge storage mechanism. **Figures 2a and 2b** show the GITT results as a function of lithium content for nanosheets and nanowires, while **Figures 2c and 2d** depict the open circuit voltage (U_{OCV}), potential (V) and entropic potential ($\partial U_{OCV}/\partial T$) derived from the analysis. In the GITT experiments, both U_{OCV} and $\partial U_{OCV}/\partial T$ varied monotonically with lithium composition, confirming that the solid-solution regime is maintained throughout the entire Li^+ (de)intercalation process.[27] In addition, both the overpotential and hysteresis of the entropic potential are larger in the case of nanosheets as compared to the nanowires, indicating better reversibility in the latter (see also **Figure S2**). These results also show that despite the clear differences in the electrochemical responses reported in the CV experiments, neither of the nanostructures undergoes any first-order phase transition, ion ordering, or amorphization upon cycling.

TT-Nb_2O_5 is well known for fast diffusion of lithium upon intercalation, even in bulk micron-sized particles.[11] As such, one could logically assume that nanostructures exposing preferential facets to the electrolyte should display comparable electrochemical performances. As discussed in the following paragraphs, this assumption holds true as long as the concentration of oxygen vacancies remains unaffected upon nanostructuring. The fact that the two nanostructured anodes performed differently upon (de)lithiation, is associated with the difference in the distribution of oxygen vacancies arising during the synthesis of the nanosheets and nanowires.

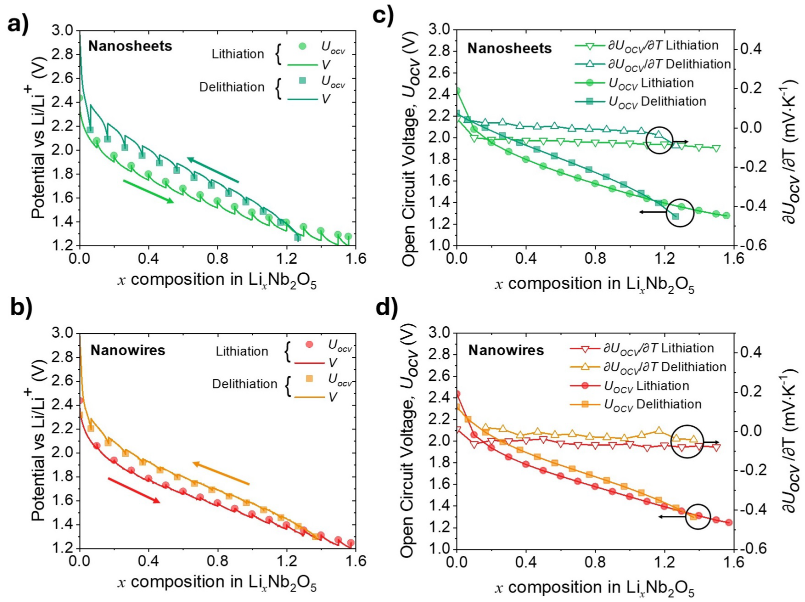

Figure 2: GITT measurements at 20 °C for TT-Nb_2O_5 a) nanosheets, b) nanowires; c) and d) depict the open circuit voltage U_{OCV} and entropic potential $\partial U_{OCV}/\partial T$ of TT-Nb_2O_5.

The sheet-like and 1-D wire morphologies of the two *TT*-Nb_2O_5 nanostructures are apparent in the SEM images (**Figures 3a and 3b**), as is their uniformity. Complementary TEM images (**Figures 3c and 3d**) indicate that both have comparable cross-sectional thickness, roughly ranging between 8 to 20 nm. Therefore, we can assume that Li^+ diffusion lengths are comparable in the two microstructures. Fast Fourier Transform (FFT) analysis (**Figures 3f and 3g**) of bright-field TEM confirmed that both nanostructures possess the *P6-mmm* symmetry of pseudohexagonal *TT*-Nb_2O_5. The nanowires grow preferentially along the [*001*] direction, while nanosheets mainly expose {*h00*} planes. Visible $d_{(100)}$ lattice fringes also revealed that the d-spacing in neighboring {*h00*} planes is slightly larger in nanowires (3.15 Å) than in nanosheets (3.12 Å), suggesting that the crystal structure is distorted by its large anisotropy.

Additional insights regarding the structures of both nanosheets and nanowires were obtained via synchrotron XRD analysis (**Figure 3e**). There is preferential orientation in the case of nanowires, where the only intense peaks are associated with (*001*) and (*002*) reflections of the *P6-mmm* structure (JCPDS card No. 07-0061). Nanosheets resulted in a larger degree of crystallinity, as nearly all diffraction peaks belonging to *TT*-Nb_2O_5 are visible. Rietveld refinement confirmed that these nanosheets preferentially expose {*h00*} facets, along with {*h0l*} and {*00l*}, suggesting that crystal growth is not highly selective (**Figure S3** and **Figure S4**). Rietveld refinement also revealed that while the unit cell in nanosheets coincides with that of the bulk *TT*-Nb_2O_5 standard (ICSD 177672), that of nanowires is expanded by 5% in volume (**Tables S1** and **S2**). Unit cell expansion is largely reported in nanoscale materials as a result of atomic structure relaxation effects and due to the presence of point defects such as oxygen vacancies.[34–36] From Raman spectroscopy (**Figure S6**) and XAS results (**Figure 4**), we attribute this lattice expansion to the presence of oxygen vacancies in the bulk of the nanowires, and not just on the surface, as expected for nanosheets.

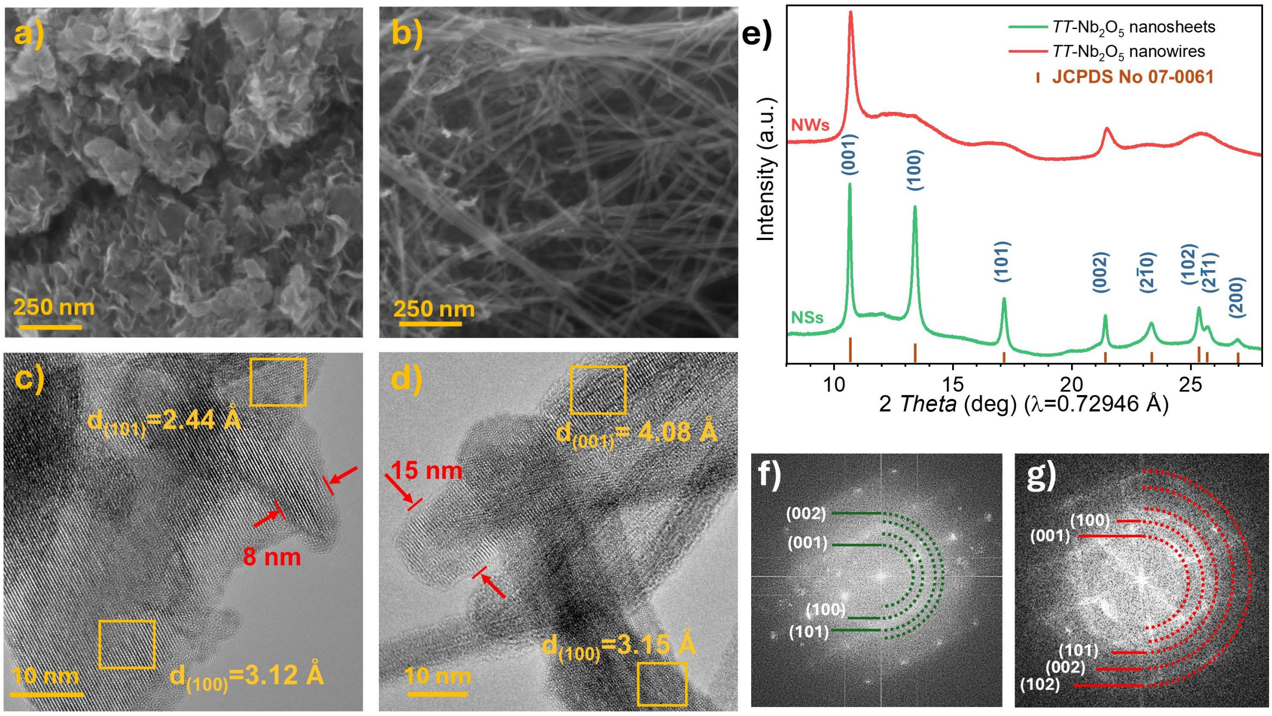

Figure 3: SEM and TEM images of a), c) nanosheets and b), d) nanowires, respectively. The observable diffraction patterns in the TEM analyses correspond to {001} and {100} planes of TT-Nb₂O₅. Accordingly, nanowires preferentially grow along the [001] direction while nanosheets mainly expose the {100} plane. e) Qualitative synchrotron XRD patterns of nanowires (red) and nanosheets (lime green) with peaks indexed to the pseudohexagonal P6/mmm structure support the preferential growth of the nanowires in the {001} direction. f) FFT image of nanosheets originated from the area selected in c. g) FFT image of nanowires originated from the areas selected in d.

Since the presence of oxygen vacancies may alter the oxidation state of a redox-active metal center, Nb K-edge XAS was used to probe the oxidation state and local site symmetry of the *TT*-Nb_2O_5 systems. **Figure 4a** shows the Nb K-edge X-ray absorption near-edge spectroscopy (XANES) spectra of *TT*-Nb_2O_5 nanowires and nanosheets along with a reference spectrum for Nb_2O_5, while **Figure 4b** shows the Fourier-transformed R-space data. The XANES (**Figure 4a**) region shows a pre-edge peak at ~ 18984 eV, which arises due to the dipole-forbidden 1*s* → 4*d* transition. In view of the fact that the structure of *TT*-Nb_2O_5 consists of corner- and edge-sharing NbO_6 and NbO_7 polyhedra that are distorted,[37] the pre-edge peaks provide a direct probe of the degree of polyhedral distortion. The intensities of the pre-edge peaks of nanowires and nanosheets are comparable to one another and greater than that of the oxide standard, thus indicating there are more distorted NbO_n polyhedra in the nanoarchitectures than in the oxide standard. Although oxygen vacancies may induce multivalence in transition metals, the edge energy (E_0) across the systems was found to be ~18992 eV, similar to the Nb_2O_5 reference standard, suggesting that the average oxidation state of Nb remained 5^+.[38] Prior research has shown that an energy gap of 3 eV is expected between Nb^{4+} and Nb^{5+} oxidation states.[39] Since the energy shifts among the nanostructures and oxide reference are less than 1 eV (**Figure S7**), there is apparently no change in the oxidation state across Nb-containing systems.

The Fourier transformed R-space spectra (**Figure 4b)** show two distinct regions: the Nb-O bonding at around 1.5 Å and the Nb-Nb nearest neighbor interactions between 2-4 Å. The amplitude reduction in the Nb-O peak in the nanosheets and nanowires suggests that the coordination number of O around Nb decreases, relative to the *T*-Nb_2O_5 standard. This is consistent with the presence of vacancies in the nanoarchitectures.[40] A lower EXAFS signal suggests more disorder in the nanowires and nanosheets than in the standard, as also reported in other systems.[41] Given that the nanowires exhibit the lowest amplitude in the signal at 1.5 Å, we can conclude that they are characterized by a larger concentration of vacancies, which is consistent with the unit cell expansion observed from XRD. Accordingly, these results suggest that vacancies permeate into the bulk structure, a feature also discussed in the Raman spectroscopy section (**Figure S6**) in the *Supplemental Information*. The Nb-Nb peaks at radial distances of ~2.9 Å and ~3.5 Å arise from the edge- (*ab*-plane) and corner-sharing (*c*-plane) polyhedra, respectively (**Figure 4c**).[42] The most noteworthy change is the variation in peak intensity in the Nb-Nb interactions at ~3.5 Å. A smaller crystallite size as observed in the nanowires and nanosheets, leads to a higher surface-to-bulk ratio as compared to the bulkier standard, resulting in more exposure of under-coordinated Nb-terminating surfaces, hence a decrease in the peak amplitude.[35] The first Nb-Nb shell at ~2.9 Å (edge-sharing polyhedra) does not show the same drop in intensity as the second shell. The nanosheets show preferred exposure of the {*100*} facet, among others, which would primarily decrease the peak amplitude of the first Nb-Nb shell. However, contrary to expectation, a small peak amplitude decrease is observed. The findings from XRD show all the other reflections expected from the *TT*-Nb_2O_5 structure, thus a higher degree of random orientation is exhibited by the nanosheets. The volume of preferred {*h00*} surfaces could, therefore, be lower than that of the nearly bulk-like surfaces, resulting in quenched surface exposure effects. The findings from EXAFS suggest that the nanowires and nanosheets both possess oxygen vacancies with respect to the standard (from the Nb-O peak amplitude decrease), with the nanowires exhibiting a larger Nb- Nb coordination along the [*00l*] direction (from the second Nb-Nb shell).

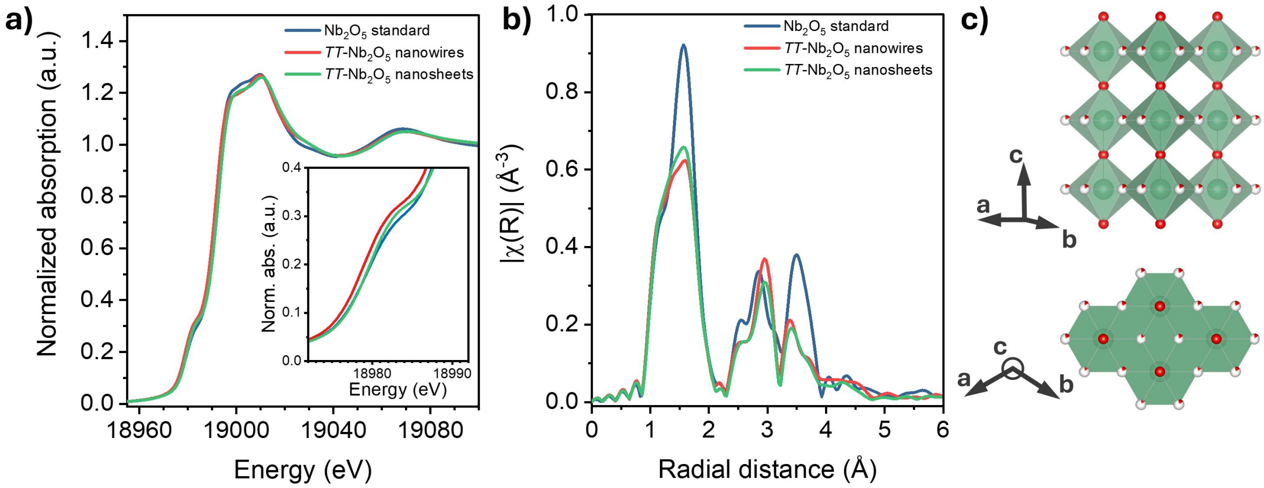

Figure 4:a) Nb K-edge XANES spectra of a reference Nb_2O_5 and TT-Nb_2O_5 nanowires and nanosheets; b) non-phase-corrected Fourier-transformed R-space data. The k-range is 3.0 to 12.0 Å-1, with dk of 1 and an arbitrary k-weight of 0.5; c) Projected TT-Nb_2O_5 structure with oxygen partial occupancies.

The XRD and XAS results are consistent with the synthetic methods used to prepare the different morphologies. The use of hexamethylenetetramine in combination with oxalic acid hinders the growth of *TT*-Nb_2O_5 nuclei along high energy facets through a multistep process controlled by surface adsorption of oxalate complexes and by pH.[19,43] As a result, growth is highly favorable along the [*00l*] direction. In fact, nanowires precipitate under hydrothermal conditions as soon as hexamethylenetetramine undergoes hydrolysis, which increases the pH concentration to controllable levels at which niobium oxalate anions dissociate and release transition metal cations. Nanosheets are formed by a different process, as a consequence of a capping effect of ethylenediamine-derived NH^{4+}, or other organic ammonium cations, to facets that expose negatively charged terminal oxygens. Crystal growth occurs in-plane under anisotropic conditions.[44] For this reason, we expect most of the induced oxygen vacancies to be located at the surface of the nanosheets and have relatively little effect on their electrochemical response. Oxygen-deficient *T*-Nb_2O_5, of which the *TT*-phase is a metastable polymorph, has been previously reported to feature enhanced (de)lithiation mechanisms.[14,37] Accordingly, our electrochemical analyses prove that, despite having comparable diffusion lengths, the *TT*-Nb_2O_5 nanowires possess better cyclability and rate capability than the nanosheets. This result is consistent with our hypothesis that oxygen vacancies which permeate the bulk crystal and induce a volumetric expansion of the unit cell are beneficial for lithium intercalation.

Surface defects cannot be neglected when studying nanostructured anodes that possess large morphological anisotropy and surface to volume ratios. For this reason, we carried out DFT calculations on the lithiation mechanism of defective *TT*-Nb_2O_5 surfaces. The pseudohexagonal structure is the least stable niobium pentoxide phase thermodynamically. A structure stacked along the *c*-axis is formed by niobium polyhedra joined by shared oxygens through the *ab*-plane (**Figure 5a**). Along a- and *b*-axes, on the other hand, a tunnel-like pattern extends across the entire structure with a diameter of about 4 Å. As previously discussed, nanowires preferentially grow along the [*001*] direction, whereas nanosheets manly expose {*100*} facets. Therefore, defective *TT*-Nb_2O_5 {*100*} and {*001*} surface models were constructed from a *TT*-Nb_2O_5 bulk structure by removing oxygen atoms, thus leaving Nb as a terminating ion, (**Figures 5b and 5c**) and accounting for crystal distortion by using unit cell parameters retrieved from our Rietveld refinement analysis (**Table S1, S2**). In particular, {*001*} facets were constructed to model surface defects in nanowires, while {*100*} was utilized to describe nanosheets. The calculated surface energy was 0.79 J m^{-2} for {*001*}, and 0.44 J m^{-2} for the {*100*} facets, respectively, while the calculated oxygen vacancy formation energy per oxygen was found to be 0.58 eV for the nanowires and 1.73 eV for the nanosheets. These values suggest that oxygen vacancies are more energetically favorable in nanowires as compared to nanosheets. We calculated the adsorption energy of Li^+ in several positions on the two surfaces and beneath the first layer of niobium atoms. The lowest adsorption energies resulted in -2.78 eV and -5.86 eV for {*100*} and {*001*} surfaces, respectively. This means that defective {*001*} surfaces are able to provide relatively stable locations for adsorbing lithium ions and that lithiation is therefore energetically more favorable than on the oxygen-deficient {*100*} surface. To be thorough, we also calculated the adsorption energy on a defective {*010*} surface resembling the lateral area of the nanowires, and values were found to be close to -2 eV. Given that the nanowires grow along the [*00l*] direction, this implies that the least exposed facets from the electrolyte are indeed the {*00l*}. Thus, their contributions to the electrochemical properties displayed by the nanowires are minimal. Overall, the DFT calculations confirm that nanostructure-induced vacancies in *TT*-Nb_2O_5 are expected to be beneficial for (de)lithiation mechanisms regardless of the exposed surface.

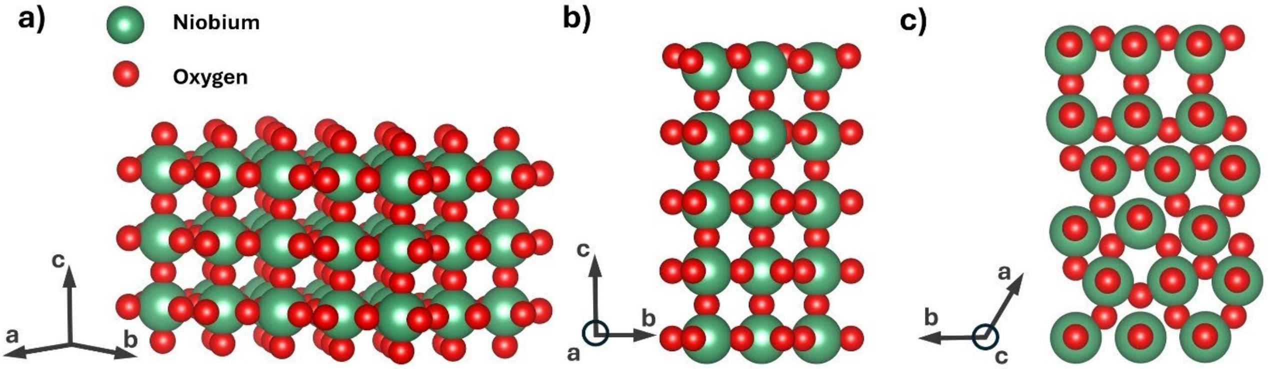

Figure 5: (a) Structure of TT-Nb_2O_5; (b) Nb-terminated {001} surface; (c)) Nb-terminated {100} surface. In all projections, vacuum is in the direction of the vertical axes. The crystal structures were visualized using Vesta.

3. Conclusions

The lithiation mechanisms of *TT*-Nb_2O_5 have been studied in relation to the disorder generated by oxygen vacancies for certain morphologies. We synthesized nanosheets whose oxygen deficiencies are mostly limited to the surface exposed to the electrolyte, and nanowires that possess vacancies permeating their bulk structure. The difference in the distribution of vacancies was validated via experimental techniques and analyzed through DFT calculations to account for surface phenomena. While the two synthesized nanostructures feature short and comparable diffusion lengths of about 5-10 nm, our results demonstrate that the distribution of vacancies is a determining factor in the electrochemical performances of *TT*-Nb_2O_5. Oxygen vacancies limited to the surface do not seem beneficial to lithium adsorption, while those reaching the bulk of the *TT*-Nb_2O_5 network induce a volume expansion of the unit cell that facilitates lithium hopping mechanisms. Moreover, our DFT calculations highlight preferential Li^+ insertion through defective {*00l*} surfaces rather than {*h00*} ones, suggesting a direction for future research on the interfacial electrochemistry of *TT*-Nb_2O_5.

Funding & Acknowledgements

This material is based upon work supported by DMREF grant #DMR 2324326. The authors would like to thank Dr. Cynthia Cibaka for providing TEM acquisitions. The authors thank the Stone Group at SSRL for the mail-in synchrotron XRD data presented in this work. Use of the Stanford Synchrotron Radiation Lightsource, SLAC National Accelerator Laboratory, is supported by the U.S. Department of Energy, Office of Science, Office of Basic Energy Sciences under Contract No. DE-AC02-76SF00515.

References

1. *Inventory of U.S. Greenhouse Gas Emissions and Sinks 1990-2022*. *EPA 430-R-24-004* https://www.epa.gov/ghgemissions/inventory-us-greenhouse-gas-emissions-and- sinks-1990-2022.%0AFOR (2024).

2. Dunn, B., Kamath, H. & Tarascon, J.-M. Electrical Energy Storage for the Grid: A Battery of Choices. *Science (1979)* **334**, 928–935 (2011).

3. Choi, C. *et al.* Achieving high energy density and high power density with pseudocapacitive materials. *Nat Rev Mater* **5**, 5–19 (2020).

4. Yan, S., Huang, R., Liu, H. & Luo, S. Remarkable Conductivity Design of $FeCo_2S_4$/MXene 2D Membrane Electrodes for Advanced Pseudocapacitance Characteristic Behavior. *ACS Appl Energy Mater* **7**, 6827–6838 (2024).

5. Yan, S. *et al.* Elevation of the Electrochemical Stability Performance of Co_3O_4/g-C_3N_4 for an Asymmetric Supercapacitor. *Energy & Fuels* **38**, 17076–17086 (2024).

6. Augustyn, V. *et al.* High-rate electrochemical energy storage through Li^+ intercalation pseudocapacitance. *Nat Mater* **12**, 518–522 (2013).

7. Lawrence, E. A. *et al.* Reversible Electrochemical Lithium Cycling in a Vanadium(IV)- and Niobium(V)-Based Wadsley–Roth Phase. *Chemistry of Materials* **35**, 3470–3483 (2023).

8. Luo, Y. *et al.* Structure and Electrochemical Properties of Bronze Phase Materials Containing Two Transition Metals. *Chemistry of Materials* **35**, 8675–8685 (2023).

9. Griffith, K. J. & Grey, C. P. Superionic Lithium Intercalation through 2×2 nm^2 Columns in the Crystallographic Shear Phase $Nb^{18}W^{8}O^{69}$. *Chemistry of Materials* **32**, 3860–3868 (2020).

10. Liu, Y., Russo, P. A., Montoro, L. A. & Pinna, N. Recent developments in Nb-based oxides with crystallographic shear structures as anode materials for high-rate lithium-ion energy storage. *Battery Energy* **2**, 1–22 (2023).

11. Griffith, K. J., Forse, A. C., Griffin, J. M. & Grey, C. P. High-Rate Intercalation without Nanostructuring in Metastable Nb_2O_5 Bronze Phases. *J Am Chem Soc* **138**, 8888–8899 (2016).

12. Han, H. *et al.* Li iontronics in single-crystalline T-Nb_2O_5 thin films with vertical ionic transport channels. *Nat Mater* **22**, 1128–1135 (2023).

13. Kim, J. W., Augustyn, V. & Dunn, B. The Effect of Crystallinity on the Rapid Pseudocapacitive Response of Nb_2O_5. *Adv Energy Mater* **2**, 141–148 (2012).

14. Zheng, Y. *et al.* Defect-Concentration-Mediated T-Nb_2O_5 Anodes for Durable and Fast-Charging Li-Ion Batteries. *Adv Funct Mater* **32**, 1–13 (2022).

15. Zhang, S., Liu, G., Qiao, W., Wang, J. & Ling, L. Oxygen vacancies enhance the lithium ion intercalation pseudocapacitive properties of orthorhombic niobium pentoxide. *J Colloid Interface Sci* **562**, 193–203 (2020).

16. Kim, H.-S. *et al.* Oxygen vacancies enhance pseudocapacitive charge storage properties of MoO_{3-x}. *Nat Mater* **16**, 454–460 (2017).

17. Zhang, H. *et al.* Layered Oxide Cathodes for Li-Ion Batteries: Oxygen Loss and Vacancy Evolution. *Chemistry of Materials* **31**, 7790–7798 (2019).

18. Wang, L., Ruan, B., Xu, J., Liu, H. K. & Ma, J. Amorphous carbon layer contributing Li storage capacity to Nb_2O_5@C nanosheets. *RSC Adv* **5**, 36104–36107 (2015).

19. Wang, X., Yan, C., Yan, J., Sumboja, A. & Lee, P. S. Orthorhombic niobium oxide nanowires for next generation hybrid supercapacitor device. *Nano Energy* **11**, 765–772 (2015).

20. Stone, K. H. *et al.* Remote and automated high-throughput powder diffraction measurements enabled by a robotic sample changer at SSRL beamline 2-1. *J Appl Crystallogr* **56**, 1480–1484 (2023).

21. Momma, K. & Izumi, F. VESTA 3 for three-dimensional visualization of crystal, volumetric and morphology data. *J Appl Crystallogr* **44**, 1272–1276 (2011).

22. Kresse, G. & Furthmüller, J. Efficiency of ab-initio total energy calculations for metals and semiconductors using a plane-wave basis set. *Comput Mater Sci* **6**, 15–50 (1996).

23. Grimme, S. Semiempirical GGA-type density functional constructed with a long-range dispersion correction. *J Comput Chem* **27**, 1787–1799 (2006).

24. Perdew, J. P., Burke, K. & Ernzerhof, M. Generalized Gradient Approximation Made Simple. *Phys Rev Lett* **77**, 3865–3868 (1996).

25. Kresse, G. & Joubert, D. From ultrasoft pseudopotentials to the projector augmented-wave method. *Phys Rev B* **59**, 1758–1775 (1999).

26. Mathew, K., Kolluru, V. S. C., Mula, S., Steinmann, S. N. & Hennig, R. G. Implicit self-consistent electrolyte model in plane-wave density-functional theory. *J Chem Phys* **151**, 234101 (2019).

27. Baek, S. W., Saber, M., Van Der Ven, A. & Pilon, L. Thermodynamic Analysis and Interpretative Guide to Entropic Potential Measurements of Lithium-Ion Battery Electrodes. *Journal of Physical Chemistry C* **126**, 6096–6110 (2022).

28. Girard, H. L., Dunn, B. & Pilon, L. Simulations and Interpretation of Three-Electrode Cyclic Voltammograms of Pseudocapacitive Electrodes. *Electrochim Acta* **211**, 420–429 (2016).

29. Chagnot, M. *et al.* Influence of Finite Diffusion on Cation Insertion-Coupled Electron Transfer Kinetics in Thin Film Electrodes. *J Electrochem Soc* **171**, 010527 (2024).

30. Li, S., Xu, Q., Uchaker, E., Cao, X. & Cao, G. Comparison of amorphous, pseudohexagonal and orthorhombic Nb_2O_5 for high-rate lithium ion insertion. *CrystEngComm* **18**, 2532–2540 (2016).

31. Meng, J. *et al.* Identification of Phase Control of Carbon-Confined Nb_2O_5 Nanoparticles toward High-Performance Lithium Storage. *Adv Energy Mater* **9**, 1–11 (2019).

32. Chen, X. *et al.* High-rate capability of carbon-coated micron-sized hexagonal TT-Nb_2O_5 composites for lithium-ion battery. *Ceram Int* **47**, 15400–15407 (2021).

33. Zhou, Y. *et al.* Synthesis of a novel hexagonal porous TT-Nb_2O_5 via solid state reaction for high-performance lithium ion battery anodes. *J Cent South Univ* **27**, 3625–3636 (2020).

34. Anspoks, A., Kalinko, A., Kalendarev, R. & Kuzmin, A. Atomic structure relaxation in nanocrystalline NiO studied by EXAFS spectroscopy: Role of nickel vacancies. *Phys Rev B* **86**, 174114 (2012).

35. Peck, M. A. & Langell, M. A. Comparison of Nanoscaled and Bulk NiO Structural and Environmental Characteristics by XRD, XAFS, and XPS. *Chemistry of Materials* **24**, 4483–4490 (2012).

36. Kuzmin, A. & Chaboy, J. EXAFS and XANES analysis of oxides at the nanoscale. *IUCrJ* **1**, 571–589 (2014).

37. Gomes, G. H. M. & Mohallem, N. D. S. Insights into the TT-Nb_2O_5 crystal structure behavior. *Mater Lett* **318**, 132136 (2022).

38. Piilonen, P. C. *et al.* Structural environment of Nb^{5+} in dry and fluid-rich (H_2O, F) silicate glasses: a combined XANES and EXAFS study. *The Canadian Mineralogist* **44**, 775–794 (2006).

39. Sanloup, C. *et al.* Behaviour of niobium during early Earth's differentiation: insights from its local structure and oxidation state in silicate melts at high pressure. *Journal of Physics: Condensed Matter* **30**, 084004 (2018).

40. Spada, D. *et al.* Spectroscopic Techniques and DFT Calculations to Highlight the Effect of Fe^{3+} on the Properties of $FeNb_{11}O_{29}$, Anode Material for Lithium-Ion Batteries. *The Journal of Physical Chemistry C* **126**, 4698–4709 (2022).

41. Xiao, Z. *et al.* Filling the oxygen vacancies in Co_3O_4 with phosphorus: an ultra-efficient electrocatalyst for overall water splitting. *Energy Environ Sci* **10**, 2563–2569 (2017).

42. SAJIKI, G. *et al.* Structural analyses and reverse Monte Carlo modeling of niobium oxide amorphous film prepared by sputtering method. *Journal of the Ceramic Society of Japan* **125**, 760–765 (2017).

43. Jehng, J. -M & Wachs, I. E. Niobium oxide solution chemistry. *Journal of Raman Spectroscopy* **22**, 83–89 (1991).

44. Su, K., Liu, H., Gao, Z., Fornasiero, P. & Wang, F. Nb_2O_5-Based Photocatalysts. *Advanced Science* **8**, 1–25 (2021).

45. Mei, B. A. *et al.* Physical Interpretations of Electrochemical Impedance Spectroscopy of Redox Active Electrodes for Electrical Energy Storage. *Journal of Physical Chemistry C* **122**, 24499–24511 (2018).

46. Altomare, A. *et al.* QUALX2.0 : a qualitative phase analysis software using the freely available database POW_COD. *J Appl Crystallogr* **48**, 598–603 (2015).

47. Coelho, A. A. TOPAS and TOPAS-Academic : an optimization program integrating computer algebra and crystallographic objects written in C++. *J Appl Crystallogr* **51**, 210–218 (2018).

48. Košutová, T. *et al.* Thermally-driven morphogenesis of niobium nanoparticles as witnessed by in-situ x-ray scattering. *Mater Chem Phys* **277**, 125466 (2022).

49. Ectors, D., Goetz-Neunhoeffer, F. & Neubauer, J. Domain size anisotropy in the double-Voigt approach: an extended model. *J Appl Crystallogr* **48**, 1998–2001 (2015).

50. Ectors, D., Goetz-Neunhoeffer, F. & Neubauer, J. A generalized geometric approach to anisotropic peak broadening due to domain morphology. *J Appl Crystallogr* **48**, 189–194 (2015).

51. Hardcastle, F. D. & Wachs, I. E. Determination of niobium-oxygen bond distances and bond orders by Raman spectroscopy. *Solid State Ion* **45**, 201–213 (1991).

52. Jehng, J. M. & Wachs, I. E. Structural Chemistry and Raman Spectra of Niobium Oxides. *Chemistry of Materials* **3**, 100–107 (1991).

53. Ravel, B. & Newville, M. ATHENA , ARTEMIS , HEPHAESTUS : data analysis for X-ray absorption spectroscopy using IFEFFIT. *J Synchrotron Radiat* **12**, 537–541 (2005).

54. Añez, R., Sierraalta, A. & Sautet, P. Structural Transformation of (110) Ultrathin Films of Tetragonal Zirconia Induced by Polarity. *The Journal of Physical Chemistry C* **111**, 8314–8320 (2007).

55. Reuter, K. & Scheffler, M. Composition, structure, and stability of (formula presented) as a function of oxygen pressure. *Phys Rev B Condens Matter Mater Phys* **65**, 1–11 (2002).

56. Stull, D. R. & Prophet, H. *JANAF Thermochemical Tables, Second Edition*. https://nvlpubs.nist.gov/nistpubs/Legacy/NSRDS/nbsnsrds37.pdf (1971) doi:10.6028/NBS.NSRDS.37.

57. Hinuma, Y. *et al.* Changes in Surface Oxygen Vacancy Formation Energy at Metal/Oxide Perimeter Sites: A Systematic Study on Metal Nanoparticles Deposited on an In_2O_3 (111) Support. *The Journal of Physical Chemistry C* **124**, 27621–27630 (2020).

Supplementary Information - Probing the effect of atomic and morphological arrangements in the pseudocapacitive properties of *TT*-Nb_2O_5 nanostructures

Andrea Zambotti[1], Gugulethu Charmaine Nkala[2], Supriti Dutta[3], Sree Harsha Bhimineni[3], Nicolas Leport[4], Aimeric Laperruque[4], Johanna Nelson Weker[2], Philippe Sautet[3], Laurent Pilon[4], Bruce Dunn[1]

[1]Department of Materials Science and Engineering, University of California, Los Angeles 90095 California, United States

[2]Stanford Synchrotron Radiation Lightsource, SLAC National Accelerator Laboratory, Menlo Park, California 94025, United States

[3]Department of Chemical and Biomolecular Engineering, University of California, Los Angeles 90095 California, United States

[4]Mechanical and Aerospace Engineering Department, Henry Samueli School of Engineering and Applied Science, University of California, Los Angeles, CA 90095, USA

Additional electrochemical results

Figure S1a shows long term cycling capacity retention at 1C over 100 cycles, while **Figure S1b** reports the Nyquist plots of the two TT-Nb_2O_5 electrodes. For both morphologies, the intercept with the real axis, corresponding to the electrode resistance, is around 5 Ω. Only one semi-circle is apparent for both morphologies.[1] That semi-circle is smaller for the electrode made of *TT*-Nb_2O_5 nanowires, indicating lower charge and mass transfer resistance.

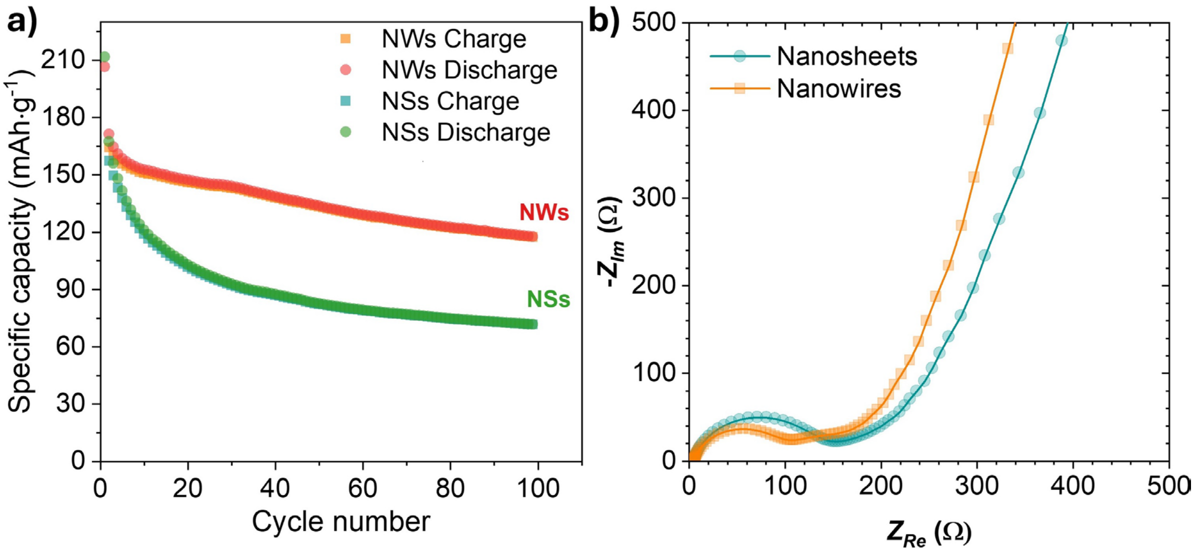

Figure S1: a) Capacity retention over 100 cycles at a rate of 1C; b) electrochemical impedance spectroscopy results plotted on a Nyquist plot for the two nanostructures in the delithiated (charged) state.

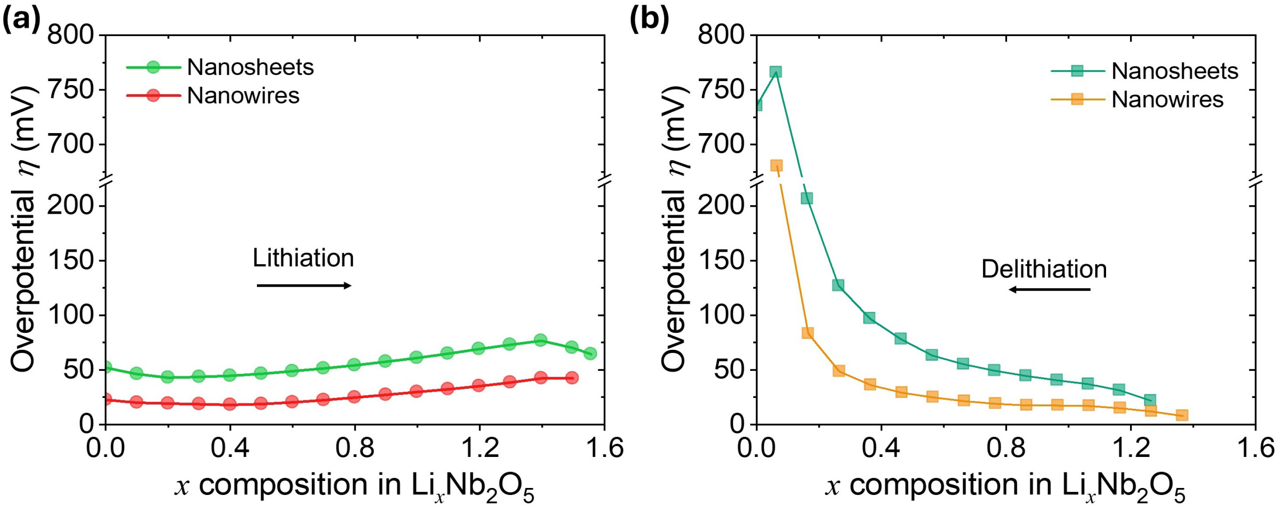

Figure S2: Values of η overpotential in the two nanostructures as a function of lithium fraction x, upon a) lithiation and b) delithiation. Scaled for comparison. The overpotential η (in mV) is given as $\eta(x) = V(x) - U_{OCV}(x)$ *where* $V(x)$ *is the measured potential and* $U_{OCV}(x)$ *the open circuit voltage.*

High-resolution XRD measurements

High-resolution XRD was performed at BL 2-1 at the Stanford Synchrotron Radiation Lightsource (SSRL), with an incident X-ray energy of 16.99 keV (λ = 0.7295 Å) in transmission mode, with a Si (111) double crystal monochromator. A Pilatus 100K area detector was used for data collection. The powdered Nb_2O_5 samples were packed into Kapton capillaries with an outer diameter of ~ 0.7 mm, sealed on both ends with clay. Phase identification was done using QualX,[2] and subsequent non-linear least squares Rietveld refinements were performed using TOPAS-Academic V7,[3] using the pseudohexagonal *P*6/*mmm* structure (ICSD Collection Code 177672) as a starting model.[4] The instrumental resolution profile was determined from LaB_6 NIST 660c standard, using the Thompson-Cox-Hastings pseudo-Voigt equation. The resulting wavelength and peak profile were kept constant during the refinements of Nb_2O_5 compositions. Lattice parameters, fractional coordinates and atomic displacement parameters were refined, with the nominal site occupancies kept constant. The sample peak broadening contributions were modeled using the anisotropic crystal size macros to account for crystallite shape-dependent anisotropic peak broadening (biaxial ellipsoid and cylinder models for the hexagonal crystal system).[5,6]

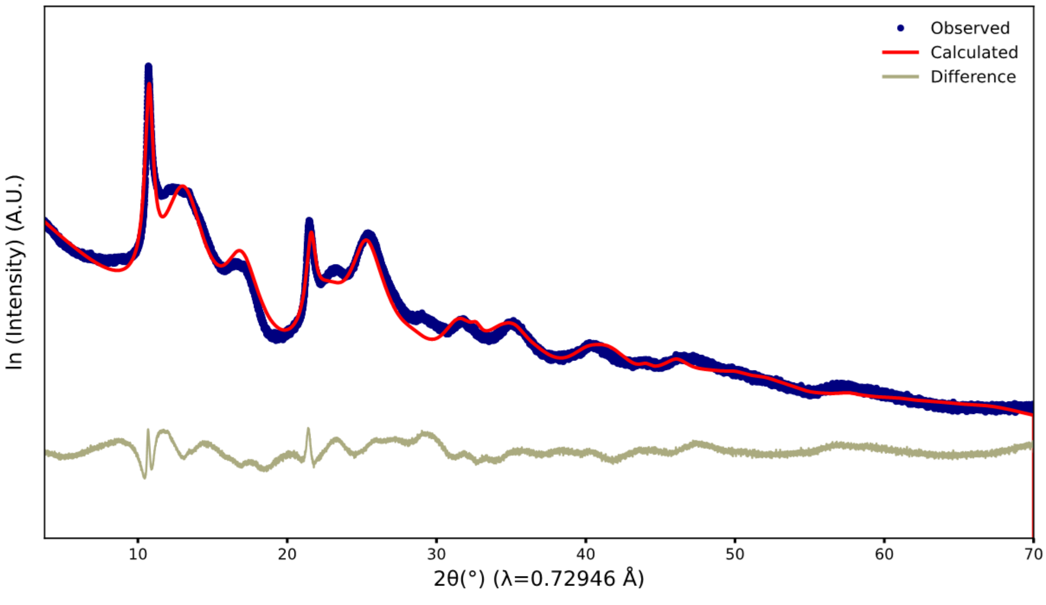

Figure S3: Rietveld refinement result of TT-Nb_2O_5 *nanowires.*

***Table S1**: Crystallographic data obtained from the Rietveld refinement of TT-Nb_2O_5 nanowires.*

TT-Nb_2O_5 (ICSD 177672)	
R_{Bragg}	2.52%
Space group	*P6/mmm*
a (Å)	3.71(1)
b (Å)	3.71(1)
c (Å)	3.893(3)
Cell volume (Å^3)	46.5(0)
Phase density (g/cm^3)	4.37(2)
Crystallite size (nm)	4.077

Whole pattern refinement parameters: R_{exp} = 26.67%, R_{wp} = 6.98%, R_p = 5.31%, GOF = 0.26.

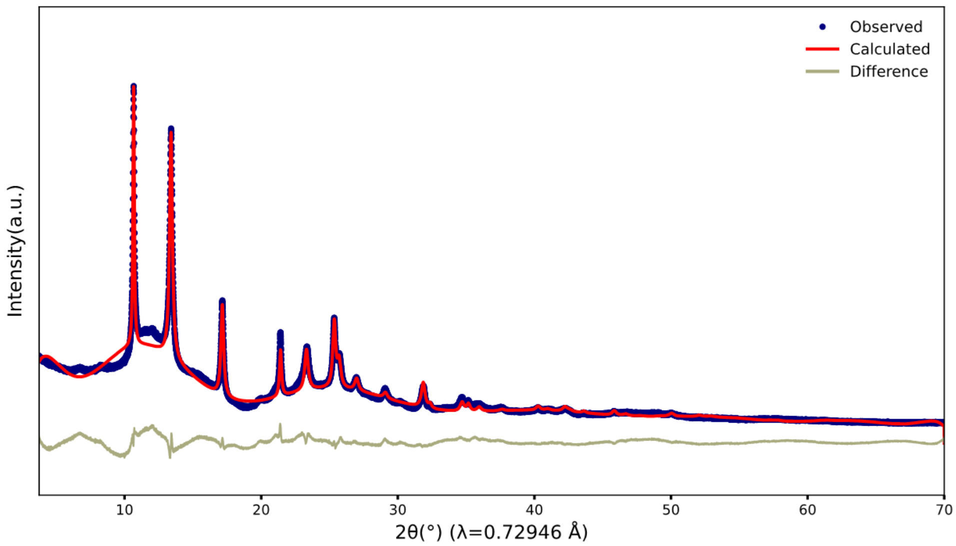

Figure S4: Rietveld refinement result of TT-Nb_2O_5 nanosheets.

***Table S2**: Crystallographic data obtained from the Rietveld refinement of TT-Nb_2O_5 nanosheets.*

TT-Nb_2O_5 (ICSD 177672)	
R_{Bragg}	2.96%
Space group	*P6/mmm*
a (Å)	3.610(1)
b (Å)	3.610(1)
c (Å)	3.926(1)

Cell volume (Å^3)	44.32(5)
Phase density (g/cm^3)	4.588(4)
Crystallite size (nm)	13.159

Whole pattern refinement parameters: R_{exp} = 26.96%, R_{wp} = 6.89%, R_p = 5.67%, GOF = 0.26.

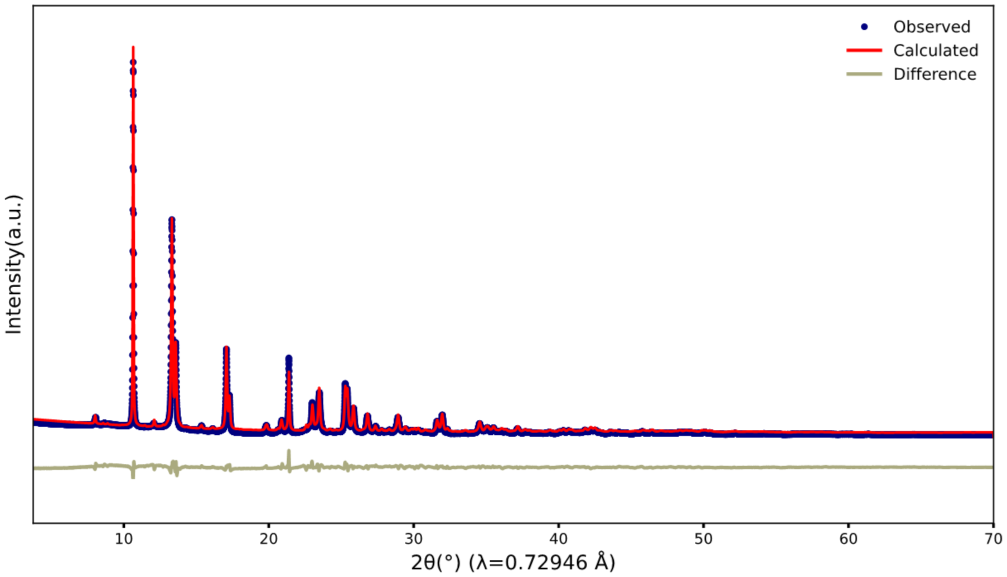

Figure S5: Rietveld refinement result of T-Nb_2O_5 reference standard used in the Nb K-edge XANES fingerprinting.

Table S3: *Crystallographic data obtained from the Rietveld refinement of T-Nb_2O_5 reference standard.*

T-Nb_2O_5 (ICSD 1840)	
R_{Bragg}	2.29%
Space group	*Pbam*
a (Å)	6.171(1)
b (Å)	29.262(4)
c (Å)	3.931(3)
Cell volume (Å^3)	709.90(1)
Phase density (g/cm^3)	5.222(1)
Crystallite size (nm)	51.228

Whole pattern refinement parameters: R_{exp} = 28.82%, R_{wp} = 7.70%, R_p = 5.88%, GOF = 0.27.

Raman Spectroscopy results

Figure S6 compares the Raman spectra of *TT*-Nb_2O_5 nanosheets, nanowires and a standard *TT*-Nb_2O_5 powder. The vibrational stretching of NbO_6 and NbO_7 polyhedra at ~700 cm^{-1} generates an asymmetric Raman peak, which accounts for a distribution in the length of Nb-O bonds.[7,8] The fact that this peak is shifted by about 10 cm^{-1} in the two spectra is evidence of the distortions occurring in the nanowires due to oxygen vacancies permeating the whole crystal structure. While a certain degree of distortion is inherent for the pseudohexagonal phase, the Raman spectrum of the nanosheets does not seem to be affected by major structural rearrangements, as the main peak falls close to that of standard *TT*-Nb_2O_5 and previously reported values for defective T-Nb_2O_5.[9] For these reasons, we can assume that the distribution of vacancies in the nanosheets is mostly limited to their exposed surfaces. These results are in agreement with the Rietveld refined unit cell volumes of the two nanostructures, where nanosheets do not seem to possess significantly distorted unit cell parameters as compared to the bulk *TT*-Nb_2O_5 standard (ICSD 177672).

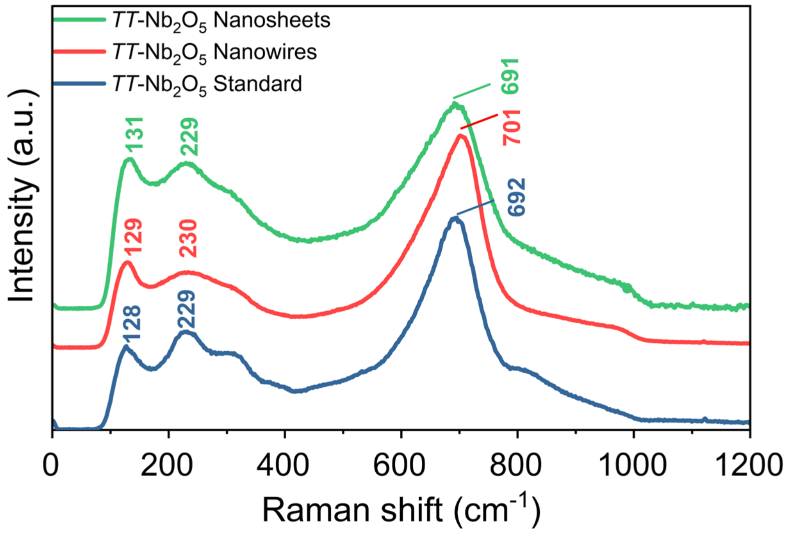

Figure S6: *Raman spectra of nanowires, nanosheets and a TT-*Nb_2O_5 *standard analyzed for comparison purposes.*

X-ray Absorption Spectroscopy measurements

All reported XAS spectra were acquired using a 2.0 T wiggler source, with the beamline being equipped with a LN_2-cooled Si (220) double-monochromator crystal at an orientation of φ = 90°. Nb K-edge spectra were measured across the edge (18 986 eV), along with a Nb foil to calibrate the energy. High-energy harmonics from the incident X-ray beam were removed by detuning the monochromator, and the energy of the incoming beam was reduced by 45%. Samples were prepared by grinding ~ 10 mg of *TT*-Nb_2O_5 along with ~ 25 mg of cellulose powder (microcrystalline 20 µm, Aldrich Chemistry) in an agate mortar and pestle into a homogeneous powder. The homogeneous powders were held between Kapton windows in an 8-slot sample holder with slot dimensions of 18 mm x 3 mm. Data were collected in transmission mode using N_2-filled ionization chambers. Data were processed and analyzed using the Demeter software suite,[10] where Athena was used for background subtraction and normalization, along with X-ray absorption near-edge structure (XANES) qualitative analysis. The absorption edge position (E_0) for every sample was determined as the maximum below 1 Å, of the first derivative (**Figure S7**). The integrated AUTOBK (Rbkg) was set to 1, to minimize background effects with a k^w of 2. The average structure of the reference oxide was *T*-Nb_2O_5 phase, as shown by Rietveld refinement (**Figure S5, Table S3**)

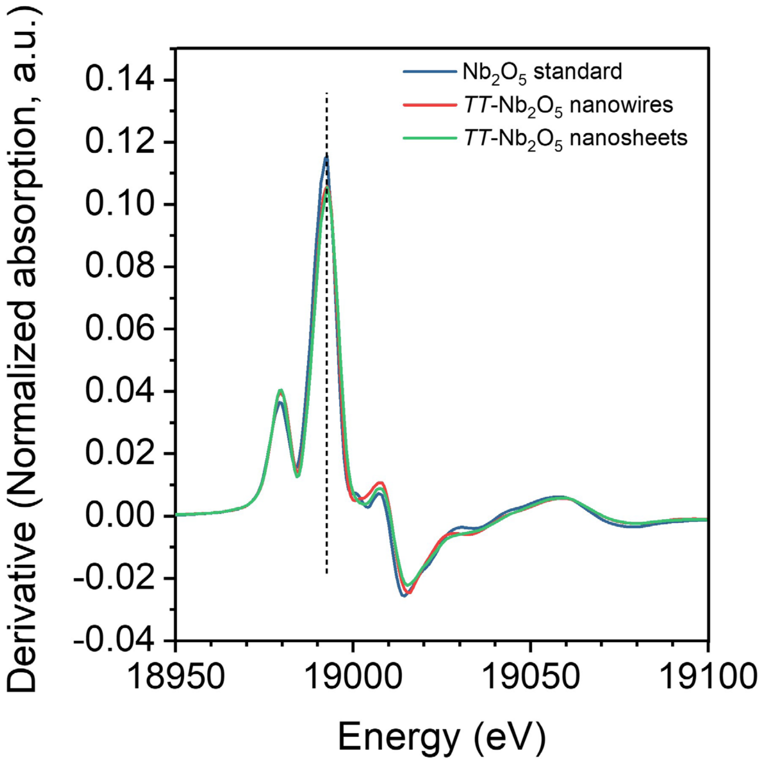

Figure S7 Normalized derivative spectra of Nb K-edge XAS of nanowires, nanosheets and the T-Nb_2O_5 standard. The line shows the maximum of the first derivative taken as E_0 to determine the average oxidation state of Nb.

Density Functional Theory computations background

All DFT calculations were performed considering the following assumptions and definitions in accordance with state-of-the-art literature sources. The surface Gibbs free energy is hereby defined as:[11,12]

$$\gamma(T,P) = \frac{1}{2A}\left[Nb_2O_5^{surface} - N_{Nb}\mu_{Nb}(T,P) - N_O\mu_O(T,P)\right] \quad (1)$$

where A is the area of the surface unit cell and N_{Nb} and N_O are the numbers of Nb and O atoms in the three-dimensional supercell, respectively. The potentials are related by the Gibbs free energy of the bulk oxide as follows:

$$2\mu_{Nb}(T,P) + 5\mu_O(T,P) = g_{Nb_2O_5}^{bulk}(T,P) \quad (2)$$

where lower case g is henceforth used to denote a Gibbs free energy per formula unit. Inserting this constraint into **Equation 1** leads to:

$$\gamma(T,P) = \frac{1}{2A}[Nb_2O_5^{surface} - \frac{N_{Nb}}{2} g_{Nb_2O_5}^{bulk}(T,P) + \left(\frac{5N_{Nb}}{2} - N_O\right)\mu_O(T,P) \quad (3)$$

Where,

$$\mu_O(T,P) = \mu_O(T,P^0) + \frac{1}{2}k_B T ln\left({}^{P}/_{P^0}\right) \quad (4)$$

Here, the oxygen chemical potential, $\mu_O(T,P)$, can be obtained using the experimental values for enthalpy and entropy at different temperatures from the NIST Databook.[13]

In our models, oxygen defects are generated by removing the terminal oxygens from the surfaces. The O vacancy formation energy is defined as:

$$E_{O_{vac}} = \frac{E_{removed} - E_{not\ removed} + \mu_O}{n} \quad (5)$$

Where E_{removed} and $E_{\text{not removed}}$ are the energies of the slab when the O atoms are removed and before removal, respectively [14]; μ_O is the oxygen chemical potential that was calculated from the energy of an isolated O_2 molecule in vacuum; n is the number of oxygen atoms in the analyzed systems. Accordingly, our models are constructed using a constant molar ratio of Nb:O=1:2.3.

References

1. Mei, B. A. *et al.* Physical Interpretations of Electrochemical Impedance Spectroscopy of Redox Active Electrodes for Electrical Energy Storage. *Journal of Physical Chemistry C* 122, 24499–24511 (2018).
2. Altomare, A. *et al.* QUALX2.0 : a qualitative phase analysis software using the freely available database POW_COD. *J Appl Crystallogr* 48, 598–603 (2015).
3. Coelho, A. A. TOPAS and TOPAS-Academic : an optimization program integrating computer algebra and crystallographic objects written in C++. *J Appl Crystallogr* 51, 210–218 (2018).
4. Košutová, T. *et al.* Thermally-driven morphogenesis of niobium nanoparticles as witnessed by in-situ x-ray scattering. *Mater Chem Phys* 277, 125466 (2022).
5. Ectors, D., Goetz-Neunhoeffer, F. & Neubauer, J. Domain size anisotropy in the double-Voigt approach: an extended model. *J Appl Crystallogr* 48, 1998–2001 (2015).
6. Ectors, D., Goetz-Neunhoeffer, F. & Neubauer, J. A generalized geometric approach to anisotropic peak broadening due to domain morphology. *J Appl Crystallogr* 48, 189–194 (2015).
7. Hardcastle, F. D. & Wachs, I. E. Determination of niobium-oxygen bond distances and bond orders by Raman spectroscopy. *Solid State Ion* 45, 201–213 (1991).
8. Jehng, J. M. & Wachs, I. E. Structural Chemistry and Raman Spectra of Niobium Oxides. *Chemistry of Materials* 3, 100–107 (1991).
9. Zheng, Y. *et al.* Defect-Concentration-Mediated T-Nb 2 O 5 Anodes for Durable and Fast-Charging Li-Ion Batteries. *Adv Funct Mater* 32, 1–13 (2022).
10. Ravel, B. & Newville, M. ATHENA , ARTEMIS , HEPHAESTUS : data analysis for X-ray absorption spectroscopy using IFEFFIT. *J Synchrotron Radiat* 12, 537–541 (2005).
11. Añez, R., Sierraalta, A. & Sautet, P. Structural Transformation of (110) Ultrathin Films of Tetragonal Zirconia Induced by Polarity. *The Journal of Physical Chemistry C* 111, 8314–8320 (2007).
12. Reuter, K. & Scheffler, M. Composition, structure, and stability of (formula presented) as a function of oxygen pressure. *Phys Rev B Condens Matter Mater Phys* 65, 1–11 (2002).
13. Stull, D. R. & Prophet, H. *JANAF Thermochemical Tables, Second Edition*. https://nvlpubs.nist.gov/nistpubs/Legacy/NSRDS/nbsnsrds37.pdf (1971) doi:10.6028/NBS.NSRDS.37.
14. Hinuma, Y. *et al.* Changes in Surface Oxygen Vacancy Formation Energy at Metal/Oxide Perimeter Sites: A Systematic Study on Metal Nanoparticles Deposited on an In 2 O 3 (111) Support. *The Journal of Physical Chemistry C* 124, 27621–27630 (2020).